

Epitaxial growth and characterization of $\text{Bi}_{1-x}\text{Sb}_x$ thin films on (0001) sapphire substrates

Yu-Sheng Huang,¹ Saurav Islam,¹ Yongxi Ou,¹ Supriya Ghosh,² Anthony Richardella,³ K. Andre Mkhoyan,² and Nitin Samarth⁴

¹*Department of Physics, Pennsylvania State University, University Park, Pennsylvania 16802, USA*

²*Department of Chemical Engineering and Materials Science, University of Minnesota, Minneapolis, Minnesota 55455, USA*

³*Department of Physics and Materials Research Institute, Pennsylvania State University, University Park, Pennsylvania 16802, USA*

⁴*Department of Physics, Department of Materials Science and Engineering, and Materials Research Institute, Pennsylvania State University, University Park, Pennsylvania 16802, USA*

(*Electronic mail: nsamarth@psu.edu)

(*Electronic mail: ski5160@psu.edu)

(Dated: 21 November 2023)

We report the molecular beam epitaxy of $\text{Bi}_{1-x}\text{Sb}_x$ thin films ($0 \leq x \leq 1$) on sapphire (0001) substrates using a thin $(\text{Bi,Sb})_2\text{Te}_3$ buffer layer. Characterization of the films using reflection high energy diffraction, x-ray diffraction, atomic force microscopy, and scanning transmission electron microscopy reveals epitaxial growth of films of reasonable structural quality. This is further confirmed via x-ray diffraction pole figures that determine the epitaxial registry between the thin film and substrate. We further investigate the microscopic structure of thin films via Raman spectroscopy, demonstrating how the vibrational modes vary as the composition changes and discussing the implications for the crystal structure. We also characterize the samples using electrical transport measurements.

I. INTRODUCTION

The $\text{Bi}_{1-x}\text{Sb}_x$ alloy first garnered significant attention in the field of semimetals and narrow bandgap semiconductors due to its electric, magnetic, and thermal properties [1–6]. While much of this past work focused on the growth and proper-

ties of bulk single crystals, the use of molecular beam epitaxy (MBE) had also been explored, demonstrating the growth of $\text{Bi}_{1-x}\text{Sb}_x$ thin films on BaF_2 and CdTe substrates [7, 8]. It has long been recognized that the energy bands of this alloy invert as a function of composition leading to an unusual gapless state at the crossing point [9, 10]. This was later understood to lead to topological surface states that were first predicted by Kane and Mele [11] and then experimentally realized in bulk single crystals [12, 13]. Recently, there has been renewed interest in thin films of $\text{Bi}_{1-x}\text{Sb}_x$ grown by both MBE [14, 15] and sputtering [16], motivated by the prospect of exploiting the spin-momentum correlation in the topological Dirac surface states for spin-orbit-torque (SOT) devices. The high electrical conductivity of $\text{Bi}_{1-x}\text{Sb}_x$ thin films coupled with a potentially large spin Hall angle makes them attractive for realizing energy efficient SOT memory devices [17]. Large spin Hall angle ≈ 52 and magnetization switching at ultralow current densities have been reported in $\text{Bi}_{1-x}\text{Sb}_x$ films interfaced with the metallic ferromagnet, MnGa [18], while interfacing with the ferromagnetic semiconductor, $(\text{Ga,Mn})\text{As}$, has shown giant unidirectional spin Hall magnetoresistance [19]. These studies motivate the further exploration of MBE growth of high-quality, single-crystal $\text{Bi}_{1-x}\text{Sb}_x$ films on different substrates. As mentioned above, attempts to grow high structural quality $\text{Bi}_{1-x}\text{Sb}_x$ thin films on BaF_2 and CdTe (111) substrates using MBE date back to the late 1990s [8]. More recent studies of MBE-grown single crystal $\text{Bi}_{1-x}\text{Sb}_x$ thin films have used GaAs (001) as a substrate, yielding $\text{Bi}_{1-x}\text{Sb}_x$ (012) growth of either polycrystalline or textured nature, with limited structural characterization details [14, 15, 18]. The renewed interest in $\text{Bi}_{1-x}\text{Sb}_x$ thin films for topological spintronics provides a strong motivation for exploring, understanding, and improving the epitaxial growth of single crystal thin films

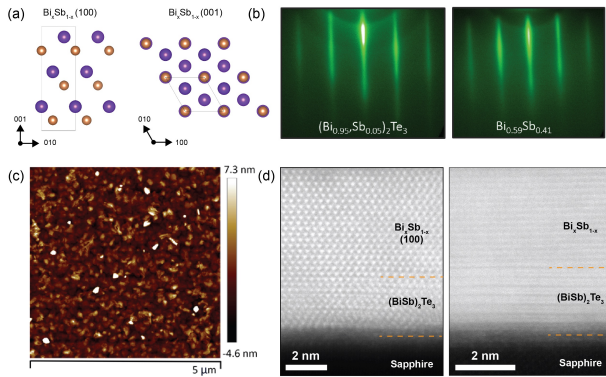


FIG. 1. (a) Schematic of the $\text{Bi}_{1-x}\text{Sb}_x$ crystal structure along the [100] direction and the [001], growth direction of the film. Violet and dark yellow correspond to Bi and Sb atoms respectively. (b) RHEED patterns of both the $\text{Bi}_{0.59}\text{Sb}_{0.41}$ layers and the $(\text{Bi}_{0.95}\text{Sb}_{0.05})_2\text{Te}_3$ buffer layer, the electron beam is directed along the $10\bar{1}$ orientation of sapphire. (c) AFM image of the $\text{Bi}_{0.59}\text{Sb}_{0.41}$ film over a $5 \mu\text{m}$ by $5 \mu\text{m}$ region. (d) HAADF-STEM image of $\text{Bi}_{0.84}\text{Sb}_{0.16}$ on $(\text{Bi}_{0.95}\text{Sb}_{0.05})_2\text{Te}_3$ buffer layer grown on sapphire substrate with the atomic structure of the film along the [100] directions as seen in the model in (a), and with a $15 - 20^\circ$ in-plane rotation in a different grain. Both show the atomically smooth interface and epitaxial growth of the layers.

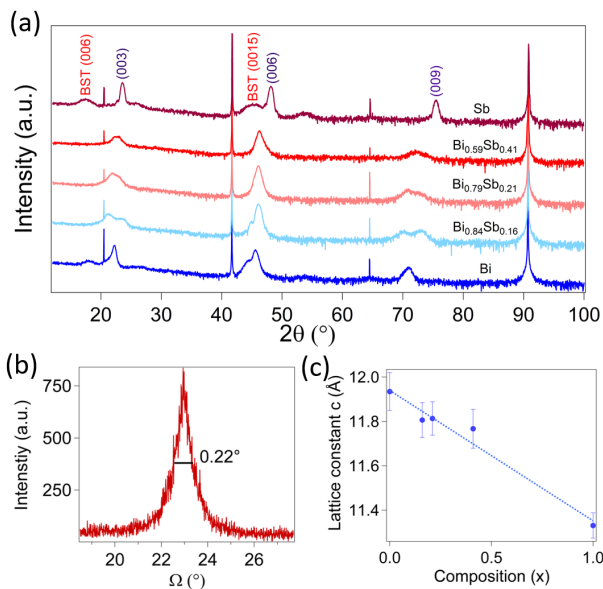


FIG. 2. (a) Out-of-plane 2θ - ω XRD measurements of 10 nm-thick $\text{Bi}_{1-x}\text{Sb}_x$ films of varying composition grown on sapphire (0001) substrates (samples A-E, as described in Table I). Peaks from the $\text{Bi}_{1-x}\text{Sb}_x$ layer, $(\text{Bi}_{0.95}, \text{Sb}_{0.05})_2\text{Te}_3$ buffer layer and the substrate layer are detected. (b) A rocking curve of $\text{Bi}_{0.84}\text{Sb}_{0.16}$. (c) Lattice constant c extracted from the 2θ - ω XRD spectrum plotted against composition. The dotted line indicates the trend suggested by Vegard's law.

of this material on different substrates.

In this manuscript, we present a comprehensive study of a series of epitaxial $\text{Bi}_{1-x}\text{Sb}_x$ thin films grown by MBE on sapphire (0001) substrates after the deposition of a thin $(\text{Bi}_{0.95}, \text{Sb}_{0.05})_2\text{Te}_3$ buffer layer. We explore the MBE growth of $\text{Bi}_{1-x}\text{Sb}_x$ thin films over the entire composition range, characterizing the microscopic structure, quality, and composition of these films with a comprehensive suite of techniques, including transmission electron microscopy (TEM), x-ray photoelectron spectroscopy (XPS), x-ray diffraction (XRD), atomic force microscopy (AFM), electrical transport, and Raman spectroscopy. The phonon modes in these thin films observed using Raman spectroscopy provide insights into the effect of strain. Our results demonstrate the growth of epitaxial $\text{Bi}_{1-x}\text{Sb}_x$ films over the full range of composition; the controlled synthesis of such films is relevant for the systematic exploration of spintronic devices based upon spin-charge interconversion in this material [20].

II. METHODS

We grow our samples on sapphire (0001) substrates using a Scienta Omicron EVO50 MBE system. We first prepare the sapphire substrates by heating up to 1160°C in air for 8 hours to produce an atomically ordered surface, dice it from the back so it can be broken into smaller pieces for future use, and clean it with a series of baths in acetone, iso-

Sample	Growth Temperature ($^\circ\text{C}$)	Bi/Sb Flux Ratio	Bi%	Sb%
A	90	Pure Bi	1	0
B	160	3.4	0.84	0.16
C	160	2.6	0.79	0.21
D	160	0.97	0.59	0.41
E	160	Pure Sb	0	1

TABLE I. Details of sample growth

propanol, DI water, Nanostrip and then DI water again. Once pieces of the substrate are loaded into the MBE system (base pressure $< 10^{-10}$ mBar), they are outgassed at a substrate heater temperature of 950°C for 1 hour. We then proceed to grow 3 nm of $(\text{Bi}_{0.95}, \text{Sb}_{0.05})_2\text{Te}_3$ (in-plane lattice constant 0.437 nm) as a buffer layer by setting the flux ratio of Bi/Sb to 19 with an overabundance of Te flux. The sample temperature is set to 170°C (as measured by an infrared thermal camera, substrate heater temperature $\approx 360^\circ\text{C}$) at the start and gradually increased to 200°C . Finally, we grow 10 nm of $\text{Bi}_{1-x}\text{Sb}_x$ with different Bi/Sb compositions by adjusting the flux ratio accordingly. A schematic of the crystal structure is shown in Fig. 1(a). $\text{Bi}_{1-x}\text{Sb}_x$ has a trigonal crystal system and belongs to $R\bar{3}m$ space group, with lattice constants $a = b = 0.433 - 0.455$ nm (depending on composition), leading to $\approx 3\%$ mismatch. The sample temperature is set at 160°C (90°C for Bi) during the growth. The lower growth temperature for pure Bi is chosen based on previous work [17], which show epitaxial growth of Bi at lower temperature. We use reflection high energy electron diffraction (RHEED) to monitor the growth. A streaky unreconstructed RHEED pattern is seen during the growth for both the buffer layer and the sample layer (Fig. 1(b)), implying a relatively smooth surface and good epitaxial growth.

We focus our discussion on five thin films with the same thickness (~ 10 nm) and different composition as determined by varying the Bi:Sb flux ratio; the sample composition is verified post-growth using x-ray photoelectron spectroscopy (XPS) (Table 1). Unlike past work on $\text{Bi}_{1-x}\text{Sb}_x$ thin films [7, 8, 15], we constrain our growth to very thin films since our primary interest is to use these films eventually in SOT devices. The thickness and surface topography of these samples are obtained using AFM, as shown in Fig. 1(c). For films of ~ 10 nm thickness, the RMS surface roughness is $\sim 1 - 2$ nm. We note that this is still somewhat above the requirements for SOT devices, but comparable to our recent work on TaAs thin films, which show giant SOT efficiency [21]. We use high angle annular dark-field (HAADF) scanning transmission electron microscopy (STEM) imaging to study the film structure from similarly grown films. Figure 1(d) shows the atomic structure of a $\text{Bi}_{1-x}\text{Sb}_x$ film along the [100] direction from different areas from the film, with the layered structure of the $(\text{Bi}_{0.95}, \text{Sb}_{0.05})_2\text{Te}_3$ buffer layer visible underneath. Further, the HAADF images show an atomically smooth interface between the $\text{Bi}_{1-x}\text{Sb}_x$ and the buffer layer, confirming a good epitaxial growth between the two.

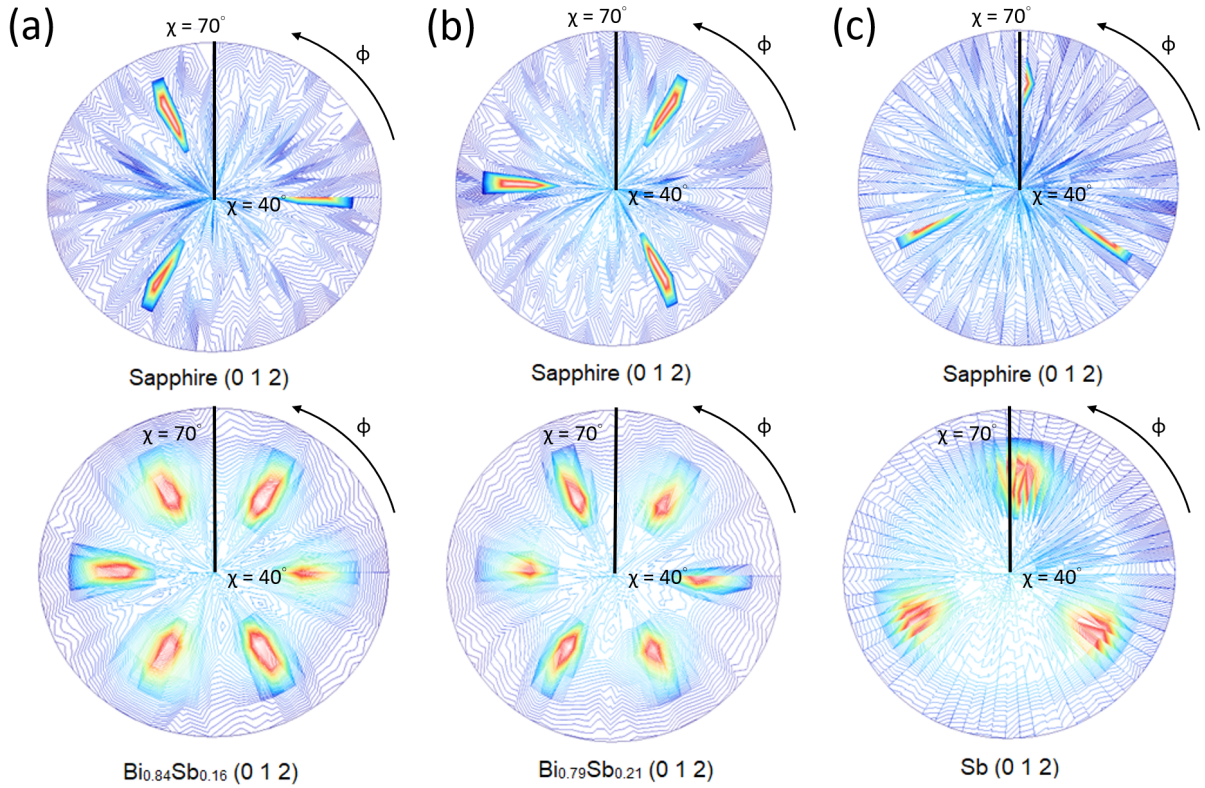


FIG. 3. XRD pole figure χ measurements of the (012) peak in both the substrate and sample layer in (a) $\text{Bi}_{0.86}\text{Sb}_{0.14}$, (b) $\text{Bi}_{0.79}\text{Sb}_{0.21}$, and (c) pure Sb.

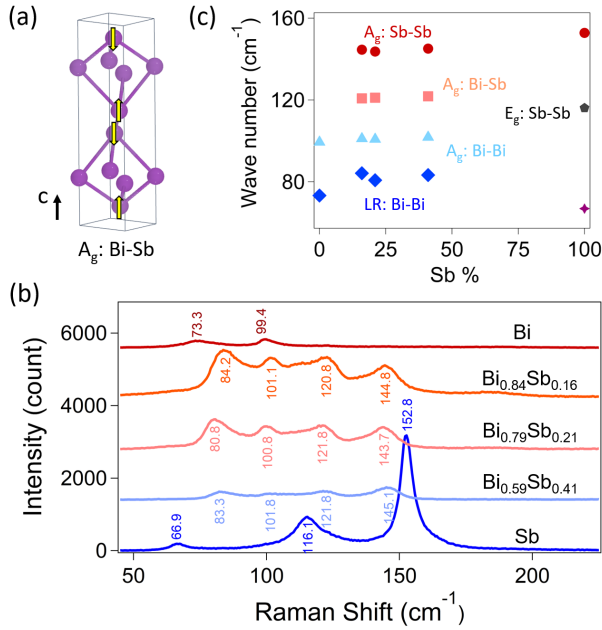


FIG. 4. (a) Schematic of the A_g vibrational mode of Bi-Sb crystal. (b) Raman spectroscopy of $\text{Bi}_{1-x}\text{Sb}_x$ films. (c) Peak location of vibrational modes versus Sb composition. LR signified long-range metal like vibration of Bi-Bi.

III. RESULTS

We first discuss the characterization of our samples using XRD measurements. Figure 2 (a) shows out of plane $2\theta - \omega$ scans of all the five films. We identify the (003) $\text{Bi}_{1-x}\text{Sb}_x$ peaks at 22° , (006) peaks at 45° - 46° , and (009) peaks at 70° - 75° . We can also identify the $(\text{Bi}_{0.95}, \text{Sb}_{0.05})_2\text{Te}_3$ (006) peak at around 18° and the (0 0 15) peak at around 52° for pure Bi and Sb films, but these peaks are absent in the alloy samples (samples B,C, and D). The reason for this is not understood. We also confirm good quality growth of our film from the rocking curve, an example of which is shown in Fig. 2(b), showing full-width at half maxima of 0.22° . The lattice constant c determined from these XRD scans shows a linear relationship with x (the percentage of Sb) in Fig. 2(c), consistent with Vegard's law [22]. However, unlike past studies of much thicker films such as $\text{Bi}_{1-x}\text{Sb}_x$ films on (111) BaF_2 [8], we find the alloys have a lattice constant which is much closer together compared to their pure counterparts. We will discuss this in more detail later in the manuscript. We further investigate these films using XRD pole figure measurements to understand the epitaxial behavior of the growth. Pole figure measurements can be understood as multiple ϕ -scans at different χ angles at a fixed $2\theta - \omega$ angle. This allows us to focus on non-out-of-plane peaks in different layers of the sample. This provides an understanding of how different layers in the film are aligned with the substrate. Ideally, we want to se-

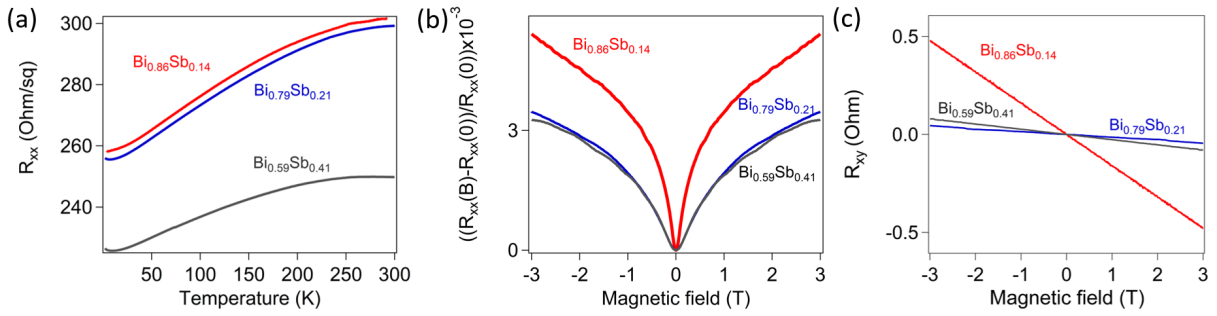


FIG. 5. Electrical transport measurements in three $\text{Bi}_{1-x}\text{Sb}_x$ films. Temperature dependence of the sheet resistance for three compositions of Bi and Sb. (b) Normalized longitudinal magnetoresistance, and (c) Transverse magnetoresistance for the same films. The raw data for R_{xx} and R_{xy} have been symmetrized and antisymmetrized, respectively.

lect reflections in all the layers with the same Miller indices, for example, (012), (104), or (110). Amongst these, (012) has the strongest signal for the $\text{Bi}_{1-x}\text{Sb}_x$ layer. Thus, we measured the (012) peaks in the substrate, $(\text{Bi}_{0.95},\text{Sb}_{0.05})_2\text{Te}_3$, and $\text{Bi}_{1-x}\text{Sb}_x$ layers (see Fig. 3). Unsurprisingly, the signal from 3 nm buffer layer was too weak to be measured. Figure 3 shows that the $\text{Bi}_{1-x}\text{Sb}_x$ film and the substrate align on top of each other with a broader ϕ spread in the sample layer. Twinning in the sample layer is observed only on the alloy samples, as shown in Figs. 3(a) and (b), with sample peaks 60° apart, and is not observed in the pure Sb sample (Fig. 3(c)). These pole figure scans confirm that the samples are epitaxial and that the pure Bi and Sb films are of higher quality than the alloyed $\text{Bi}_{1-x}\text{Sb}_x$ films.

For further understanding of the lattice dynamics, we investigate the vibrational modes of the films using Raman spectroscopy. Raman spectra of single crystals of $\text{Bi}_{1-x}\text{Sb}_x$ were first investigated by Zitter and Watson [23]. Lannin further investigated sputtered $\text{Bi}_{1-x}\text{Sb}_x$ thin films in 1979 [24]. Both results found five vibrational modes in $\text{Bi}_{1-x}\text{Sb}_x$ alloys: A_g and E_g mode of Sb-Sb vibration, A_g mode of Bi-Sb vibration, A_g mode of Bi-Bi vibration, and long-range metallic-like Bi-Bi vibration. The A_g vibrational mode of the Bi-Sb is shown schematically in Fig. 4(a). The Raman spectra in our films are shown in Fig. 4(b) and the wavenumber of different modes is plotted against composition in Fig. 4(c). We identify the long-range metal-like Bi-Bi vibration mode (blue diamonds) at 73.3 cm^{-1} in the pure Bi sample and $80 - 84\text{ cm}^{-1}$ in $\text{Bi}_{1-x}\text{Sb}_x$ alloy samples; this mode shifts to higher wave number as Sb concentration increases. The A_g mode of the Bi-Bi vibration (blue triangles) is observed around 100 cm^{-1} for all samples except in the pure Sb sample; this mode remains constant as the Sb fraction changes in the alloy samples (samples B, C, and D). The A_g mode of the Bi-Sb vibration (orange squares) is observed around 120 cm^{-1} for all $\text{Bi}_{1-x}\text{Sb}_x$ alloy samples; this mode also remains at approximately the same location as the composition is varied in the alloy samples. The E_g mode of the Sb-Sb vibration (black pentagon) is only observed at 116.1 cm^{-1} in pure Sb; this is most likely due to the lack of enough Sb concentration in the alloy samples. The A_g mode of the Sb-Sb vibration (red circles) is observed at 152.8 cm^{-1} in the pure Sb sample and at 145 cm^{-1} in

$\text{Bi}_{1-x}\text{Sb}_x$ alloy samples; this shows similar behavior as the A_g mode of the Bi-Bi vibration, and remains approximately at the same position in samples B, C, D, with the mode in the pure Sb film observed at higher wave number. Furthermore, we also identify an extra mode at 66.9 cm^{-1} (purple stars) in the pure Sb film. This mode does not correspond to any mode previously observed in single crystal $\text{Bi}_{1-x}\text{Sb}_x$ alloys. We believe this corresponds to the A_g mode from Sb_2Te_3 , suggesting the interdiffusion of Te from the $(\text{Bi}_{0.95},\text{Sb}_{0.05})_2\text{Te}_3$ buffer layer. In previous studies, the wave number of the A_g modes had a linear relationship with the composition of the Sb [23, 24]. In our study, we observe these modes to be located at approximately the same wave number. Our alloy films have a similar lattice constant c , as calculated from XRD measurements (Fig. 2(b)). The A_g mode vibrations are along the c direction as shown in the schematic in Fig. 4(a), and thus the wave number of the vibrations also correspond to the lattice constant c . This can further be seen in Fig. 2(b), where sample C(79:21) has a slightly larger lattice constant c compared to sample B(84:16) and similarly we also observe a slightly smaller wave number of the A_g in sample C compared to sample B. We believe this is because presence of strain in our sample [25].

Finally, we investigate electrical transport in $\text{Bi}_{1-x}\text{Sb}_x$ thin films of varying composition grown under similar conditions. We carry out these measurements using mechanically scratched Hall bars with channel dimensions $1\text{ mm} \times 500\text{ }\mu\text{m}$. The films show similar qualitative and quantitative behavior. The sheet resistance (R_{xx}) vs. temperature (T) in all samples shows metallic behavior (Figs. 5(a)). Longitudinal magnetoresistance measurements at $T = 4.2\text{ K}$ shows a positive magnetoresistance whose field-dependence is consistent with that expected from weak antilocalization (Figs. 5(b)). The carrier density (n) for all the samples is extracted using Hall measurements (Figs. 5(c)). The samples are electron-doped with $n \approx 10^{20} - 10^{22}\text{ cm}^{-3}$. The mobility is calculated using $\mu = \frac{\sigma}{ne}$, where σ is the conductivity and e is the electronic charge. The Fermi wavelength (k_f), calculated using $k_f = (3\pi^2n)^{\frac{1}{3}}$ is $\approx 10^{-9}\text{ m}^{-1}$ while the mean free path (l_m), calculated using $l_m = \mu\hbar k_f/e$ varies between $10^{-8} - 10^{-9}\text{ m}$. $k_f l_m$ varies between $10 - 25$ in these films. The parameters calculated from transport measurements are provided in Table

Sample	n (cm ⁻³)	μ (cm ² /Vs)	k_f (10 ⁹ m ⁻¹)	l_m (m)	$k_f l_m$
A	-2.48×10^{21}	1	9	5.2×10^{-10}	4.7
B	-1.9×10^{21}	12.7	3.8	3.2×10^{-9}	12.3
C	-5.7×10^{20}	67.7	2.4	1.07×10^{-9}	25.8
D	-1.28×10^{22}	2.2	7.18	1.04×10^{-9}	7.5
E	-6.7×10^{20}	51.4	2.7	9.1×10^{-9}	24.8

TABLE II. Details of transport measurements

II. Note that the relatively low Hall mobilities extracted here can be attributed to the thin nature of our films, where interfacial defects which act as trapping-detraping centers [26] and grain boundaries from twinning as observed in XRD (Fig. 3), can lead to enhanced scattering compared to thicker films: for example, the MBE growth of Bi_{1-x}Sb_x thin films of about 60 nm thickness on GaAs substrates also shows Hall mobilities of order 100 cm²/(V.s) [15].

IV. CONCLUSION

In conclusion, we used MBE to demonstrate the epitaxial growth of a series of Bi_{1-x}Sb_x thin films over the entire alloy composition range on sapphire (0001) substrates with a thin (Bi_{0.95}Sb_{0.05})₂Te₃ buffer layer. Detailed structural characterization of the films via XRD and HR-TEM confirm high-quality epitaxial registry with the substrate, while the composition of these films was verified using XPS. We also probed the effect of strain (and possible interdiffusion) using Raman spectroscopy and probed their electrical properties using low temperature transport. Our growth protocol establishes sapphire (0001) as an attractive substrate for MBE growth of Bi_{1-x}Sb_x and provides a route for systematic studies of the spin-charge conversion and SOT devices by interfacing such films with a ferromagnetic overlayer [20].

ACKNOWLEDGMENTS

This project was supported by SMART, one of seven centers of nCORE, a Semiconductor Research Corporation program, sponsored by the National Institute of Standards and Technology (NIST) (YS, YO, NS, SG, KAM), NSF Grant No. DMR-2309431 (SG, KAM), and by the Penn State Two-Dimensional Crystal Consortium-Materials Innovation Platform (2DCC-MIP) under NSF Grant No. DMR-2039351 (YO, SI, AR, NS). Parts of this work were carried out in the Characterization Facility, University of Minnesota, which receives partial support from the NSF through the MRSEC (Award Number DMR-2011401) and the NNCI (Award Number ECCS-2025124) programs (SG, KAM).

- ¹E. Mendez, A. Misu, and M. Dresselhaus, "Pressure-dependent magnetoreflection studies of Bi and Bi_{1-x}Sb_x alloys," *Phys. Rev. B* **24**, 639 (1981).
- ²N. Brandt, E. Svistova, and R. Valeev, "Investigation of the semiconductor-metal transition in the bismuth-antimony system in a magnetic field," *Sov. Phys. JETP* **28**, 245–254 (1969).
- ³N. Brandt and E. Svistova, "Electron transitions in strong magnetic fields," *J. of Low Temp. Phys.* **2**, 1–35 (1970).

- ⁴N. Brandt, E. Svistova, and M. Semenov, "Electron transitions in antimony-rich bismuth-antimony alloys in strong magnetic fields," *Sov. Phys. JETP* **32**, 238–243 (1971).
- ⁵K. Hiruma, G. Kido, K. Kawachi, and N. Miura, "Shubnikov-de Haas effect and semimetal-semiconductor transition in bismuth-antimony alloys in high magnetic fields," *Solid State Commun.* **33**, 257–260 (1980).
- ⁶W. Yim and A. Amith, "Bi-sb alloys for magneto-thermoelectric and thermomagnetic cooling," *Solid-State Electronics* **15**, 1141–1165 (1972).
- ⁷D. T. Morelli, D. L. Partin, and J. Heremans, "Galvanomagnetic properties of single-crystal bismuth-antimony thin films," *Semicon. Sci. Technol.* **8**, 369–420 (1972).
- ⁸S. Cho, A. DiVenere, G. K. Wong, J. B. Ketterson, and J. R. Meyer, "Molecular beam epitaxial growth and structural properties of BiSb alloy thin films on CdTe (111) substrates," *J. Vac. Sci. Tech. A* **17**, 9–13 (1999).
- ⁹N. Brandt, S. Chudinov, and V. Karavaev, "Investigation of gapless states in bismuth-antimony alloys under pressure," *Sov. Phys. JETP* **34**, 368–375 (1972).
- ¹⁰N. Brandt, Y. G. Ponomarev, and S. Chudinov, "Investigation of the gapless state in bismuth-antimony alloys," *J. Low Temp. Phys.* **5**, S257 (1990).
- ¹¹C. L. Kane and E. J. Mele, "Z₂ topological order and the quantum spin Hall effect," *Phys. Rev. Lett.* **95**, 146802 (2005).
- ¹²D. Hsieh, D. Qian, L. Wray, Y. Xia, Y. S. Hor, R. J. Cava, and M. Z. Hasan, "A topological Dirac insulator in a quantum spin Hall phase," *Nature (London)* **452**, 970–974 (2008).
- ¹³D. Hsieh, Y. Xia, L. Wray, D. Qian, A. Pal, J. Dil, J. Osterwalder, F. Meier, G. Bihlmayer, C. Kane, *et al.*, "Observation of unconventional quantum spin textures in topological insulators," *Science* **323**, 919–922 (2009).
- ¹⁴K. Yao, N. H. D. Khang, and P. N. Hai, "Influence of crystal orientation and surface termination on the growth of BiSb thin films on GaAs substrates," *J. Cryst. Growth* **511**, 99–105 (2019).
- ¹⁵D. Sadek, R. Daubriac, C. Durand, R. Monflier, Q. Gravelier, A. Proietti, F. Cristiano, A. Arnoult, and S. R. Plissard, "Structural and electrical characterizations of BiSb topological insulator layers epitaxially integrated on GaAs," *Crystal Growth & Design* **22**, 5081–5091 (2022).
- ¹⁶T. Fan, M. Tobah, T. Shirokura, N. H. D. Khang, and P. N. Hai, "Crystal growth and characterization of topological insulator BiSb thin films by sputtering deposition on sapphire substrates," *Jpn. J. Appl. Phys.* **59**, 063001 (2020).
- ¹⁷Y. Ueda, N. H. Duy Khang, K. Yao, and P. N. Hai, "Epitaxial growth and characterization of Bi_{1-x}Sb_x spin Hall thin films on GaAs (111) A substrates," *Appl. Phys. Lett.* **110**, 062401 (2017).
- ¹⁸N. H. D. Khang, Y. Ueda, and P. N. Hai, "A conductive topological insulator with large spin hall effect for ultralow power spin-orbit torque switching," *Nat. Mater.* **17**, 808–813 (2018).
- ¹⁹N. H. Duy Khang and P. N. Hai, "Giant unidirectional spin hall magnetoresistance in topological insulator-ferromagnetic semiconductor heterostructures," *J. Appl. Phys.* **126**, 233903 (2019).
- ²⁰Y. Ou, W. Yanez, Y.-S. Huang, S. Ghosh, C. Sahin, M. Stanley, S. Islam, S. Santhosh, A. Richardella, K. A. Mkhoyan, M. E. Flatte, and N. Samarth, "Spin Hall conductivity in Bi_{1-x}Sb_x as an experimental test of bulk-boundary correspondence," *arXiv*, xxxx (2023).
- ²¹W. Yanez, Y. Ou, R. Xiao, S. Ghosh, J. Dwivedi, E. Steinebronn, A. Richardella, K. A. Mkhoyan, and N. Samarth, "Giant dampinglike-torque efficiency in naturally oxidized polycrystalline TaAs thin films," *Phys. Rev. Appl.* **18**, 054004 (2022).
- ²²A. R. Denton and N. W. Ashcroft, "Vegard's law," *Phys. Rev. A* **43**, 3161 (1991).
- ²³R. Zitter and P. Watson, "Raman and x-ray spectra of single-crystal Bi-Sb alloys," *Physical Review B* **10**, 607 (1974).
- ²⁴J. S. Lannin, "First-order Raman scattering in Bi_{1-x}Sb_x alloys," *Physical Review B* **19**, 2390 (1979).
- ²⁵Z. H. Ni, T. Yu, Y. H. Lu, Y. Y. Wang, Y. P. Feng, and Z. X. Shen, "Uniaxial strain on graphene: Raman spectroscopy study and band-gap opening," *ACS nano* **2**, 2301–2305 (2008).
- ²⁶S. Islam, S. Shamim, and A. Ghosh, "Benchmarking noise and dephasing in emerging electrical materials for quantum technologies," *Advanced Materials* **35**, 2109671.